Proceedings of the 16th European VLBI Network Symposium
Ros, E., Benke, P., Dzib, S., Rottmann, I., & Zensus, J.A. (eds.)
September 2nd-6th 2024, Bonn, Germany

A Distance Measurement for a Blazar TXS 0506+056 Using its Radio Variability and VLBI Images

Chanwoo Song[1,2] and Sang-Sung Lee[1,2]

[1] Korea Astronomy and Space Science Institute, 776 Daedeokdae-ro, Daejeon, 34055, South Korea
[2] Korea University of Science and Technology, 217 Gajeong-ro, Yuseong-gu, Daejeon 34113, South Korea

Abstract. We present the result of constraining the angular diameter distance to a blazar TXS 0506+056 ($z = 0.3365$), a radio-bright active galactic nucleus (AGN) whose jet is aligned with the line of sight. We used the 15 GHz Very Long Baseline Array (VLBA) data from MJD 54838 to MJD 60262 (15 years) and the 15 GHz Owens Valley Radio Observatory (OVRO) 40 m single dish (SD) data from MJD 54474 to MJD 59023 (12 years). The VLBA core flux density varies from 0.169 ± 0.005 Jy to 1.906 ± 0.157 Jy and the OVRO SD flux density ranges from 0.29 ± 0.03 Jy to 2.44 ± 0.03 Jy. We used a variability timescale (τ) and a causality argument of a linear size $R = c\delta\tau/(1+z)$ (taking into account a Doppler factor δ and a cosmological redshift z) to measure the angular diameter distance ($D_{\rm A} = R/\theta_R$) to the source (with its angular size θ_R). To constrain the Doppler factor, we applied the relation between the rest frame brightness temperature of an emission region ($T_{\rm b}^{\rm em}$) and the observed brightness temperature by the receiver ($T_{\rm b}^{\rm rec}$) given by $T_{\rm b}^{\rm em} = T_{\rm b}^{\rm rec}(1+z)/\delta$. We assume that $T_{\rm b}^{\rm em}$ is saturated to the intrinsic brightness temperatures $T_{\rm b,int}$ when the flare of the emission region peaks. We supposed three intrinsic brightness temperature such as the equipartition brightness temperature ($T_{\rm b,int} = 5 \times 10^{10}$ K) and the mean brightness temperatures of distributions from VLBA samples ($T_{\rm b,int} = 6.61^{+0.47}_{-0.44} \times 10^{10}$ K) and OVRO samples ($T_{\rm b,int} = 3.08 \pm 0.80 \times 10^{11}$ K) at Hubble constant $H_0 = 67.4 \pm 0.5$ km/s/Mpc with a matter density parameter $\Omega_{\rm M} = 0.315 \pm 0.007$. To calculate $T_{\rm b}^{\rm rec}$, a flux density variation and an angular size of the emission region are required. The angular size θ_R of the emission region (i.e., the VLBA core) is obtained from a circular Gaussian modelfit parameter $\theta_{\rm FWHM}$ ($\theta_R = 0.8\theta_{\rm FWHM}$), ranging in 0.036—0.228 milli–arcsecond (mas), and its uncertainty is determined to be 1.78—13.4 %. We considered the core flux density enhancement is equivalent to the difference between the maximum and the minimum flux density in a flaring period. Using the OVRO light curve, we estimated a variability timescale of $\tau = 223.94^{+0.55}_{-0.38}$ days for the giant flare in 2020 February. By fitting circular Gaussian model components to the VLBA images, we found that the variability of the VLBA core drives the giant flare. With same timescale and core flux density variation, we calculate the angular diameter distance $D_{\rm A} = R/\theta_R$, along core sizes. At ΛCDM model, the angular diameter distance of TXS 0506+056 is determined as $D_{\rm A} = 1027.5 \pm 7.6$ Mpc. From MJD 58230 to MJD 59207, we found the consistent distance measurement results with ΛCDM model within the uncertainty 11.07—24.25 %.

1. Introduction

The ΛCDM model is a well constrained cosmological model to explain the expansion of the universe and to estimate a cosmological distance. The angular diameter distance $D_{\rm A}$ is defined z as

$$D_{\rm A} = \frac{c}{H_0(1+z)} \int_0^z \frac{{\rm d}z'}{\sqrt{\Omega_{\rm M}(1+z')^3 + (1-\Omega_{\rm M})}}, \qquad (1)$$

where H_0 is the Hubble constant and $\Omega_{\rm M}$ is the matter density parameter (Verde, Schöneberg & Gil-Marín 2024). To infer H_0 and $\Omega_{\rm M}$, the cosmic distance ladder can be used, being broadly divided into two categories such as the direct distance ladder and the inverse distance ladder. The direct distance ladder determines the distance from specific celestial objects such as Cepheid variables, Type Ia supernovae (SNe Ia) and red giant branch (RGB, i.e., tip of RGB). The inverse distance ladder infer the cosmological parameters by observing the early time processes such as the cosmic microwave background (CMB) and the baryonic acoustic oscillation (BAO). However, nowadays, there is a discrepancy of H_0 inference constrained by both distance ladders, that is called as the Hubble tension problem. The direct distance ladder yields $H_0 = 73.04 \pm 1.04$ km/s/Mpc (Riess et al. 2022), whereas the inverse distance ladder yields $H_0 = 67.4 \pm 0.5$ km/s/Mpc (Aghanim et al. 2020). Solving the Hubble tension is very difficult at the moment. One of the tasks for solving the Hubble tension is expanding the local limits of the direct distance ladder, because the direct distance ladder obviously has a fatal flaw in higher redshifts. Among the rungs in the direct distance ladder, SNe Ia are known as the farthest rung reaching up to $z = 2.26$ (Scolnic et al. 2018). It is difficult to observe distant objects because the intensity dims by $(1+z)^3$ as a function of z. If the cause of the Hubble tension is due to the locality of the direct distance ladder, finding new lungs of the ladder with higher redshift may be a clue. Blazars are a subclass of active galactic nuclei (AGNs) where relativistic jets powered by a supermassive black

Morphologies	K	M
Uniform Disk	π	0.8
Sphere	$2\pi/3$	0.9

Table 1: Values of K and M factors from Equation 2 for different emission region morphologies

hole (SMBH) at the center are observed, being closely aligned to the line of sight. When the relativistic particles in the jet pass through the magnetic field, the synchrotron radiation is emitted in a wide range of electromagnetic wave from radio to gamma-ray. The synchrotron radiation is Doppler–boosted by the relativistic effect and hence can be observed from the distant blazars in high redshift. Especially, the very long baseline interferometry (VLBI) allows obtaining high–resolution images of the blazars on parsec scales and measuring accurate angular sizes. The high redshift blazars above 6.10 can be imaged by the VLBI (Zhang et al. 2022). In Equation 8 of Hodgson et al. 2023, a method of distance determination is suggested using Doppler–boosted celestial objects (e.g., blazars). We introduced the scaling factor g, K and M, and corrected that equation as following (Equation 2)

$$D_{\rm A} = \frac{c^3}{2k_{\rm B}T_{\rm b,int}\nu^2}\frac{g\tau\Delta S_\nu}{K(M\theta_{\rm FWHM})^3}, \quad (2)$$

where c is the speed of light, $k_{\rm B}$ is the Boltzmann constant, $T_{\rm b,int}$ is an intrinsic brightness temperature, ν is an observed radio frequency, ΔS_ν is an observed spectral flux density variation, τ is an observed radio variability timescale and $\theta_{\rm FWHM}$ is an angular full width half maximum (FWHM) of a circular Gaussian. The scaling factors g and K are given by Equation 3 (Hodgson et al. 2023) and Equation 4, respectively, and M is given by $\theta_R = M\theta_{\rm FWHM}$

$$\theta_R = \frac{R}{D_{\rm A}} = g\frac{c\delta\tau_\nu}{(1+z)D_{\rm A}}, \quad (3)$$

$$S_\nu = 2\pi\int_0^{\theta_R} I_\nu(\theta)\sin\theta{\rm d}\theta = K\theta_R^2 I_\nu(0), \quad (4)$$

where θ_R is an angular size of an emission region, δ is the Doppler factor, and $I_\nu(\theta)$ is a spectral intensity whose distribution is cylindrically symmetric.

TXS 0506+056 is a blazar classified as an intermediate–spectral peaked BL Lac object AGN ($z = 0.3365$). The neutrino event (IceCube-170922A) was reported in 2017 September (Hovatta et al. 2021) and a γ–ray flaring was also detected by The Fermi Large Area Telescope (LAT) in almost same period (Abdollahi et al. 2023). In 2020 May, the 15 GHz radio flux density reached the maximum of 2.44 Jy observed by Owens Valley Radio Observatory (OVRO) 40 m radio telescope (Hovatta et al. 2021). We applied Equation 2 to TXS 0506+056 in order to examine if blazars can be used as a valid means for distance measurements.

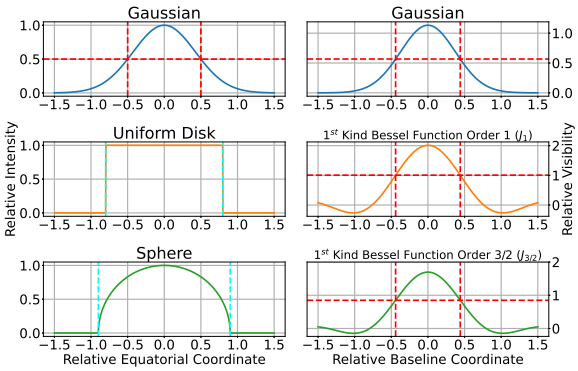

Fig. 1: Theoretical visibility distributions (right) matching intensity distributions (left). Red dashed lines represent FWHM, cyan dashed lines indicate radius. Solid lines (blue, orange, green) depict Gaussian, uniform disk, and sphere intensity distributions, respectively. All distributions share the same FWHM.

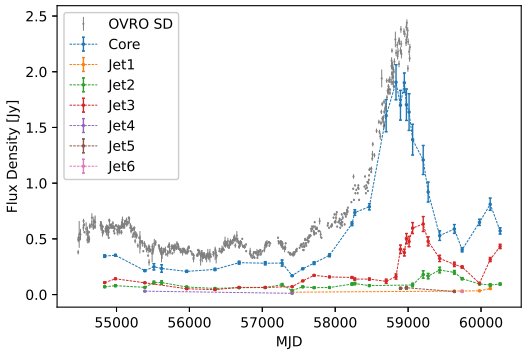

Fig. 2: Flux density curves for circular Gaussian model components of the VLBA (Core, Jet1 to Jet6, colored) and OVRO SD (gray).

2. Data Analysis

To determine emission region size, we used 15 GHz Very Long Baseline Array (VLBA) data from MJD 54838 to MJD 60262 (15 years) which is a part of the Monitoring Of Jets in Active galactic nuclei with VLBA Experiments, i.e., MOJAVE (Lister et al. 2018). To measure timescales of the flares, we used 15 GHz Owens Valley Radio Observatory (OVRO) 40 m single dish (SD) data from MJD 54474 to MJD 59023 (12 years) (Richards et al. 2011). Since the OVRO SD data have a mean cadense of 7 days.

2.1. Circular Gaussian fitting to 15 GHz VLBA data from MOJAVE

To measure the angular sizes of the emission region, we fitted the 2D circular Gaussian model to the 15 GHz VLBA data by using Difmap. We performed the model fitting with increasing the number of model components

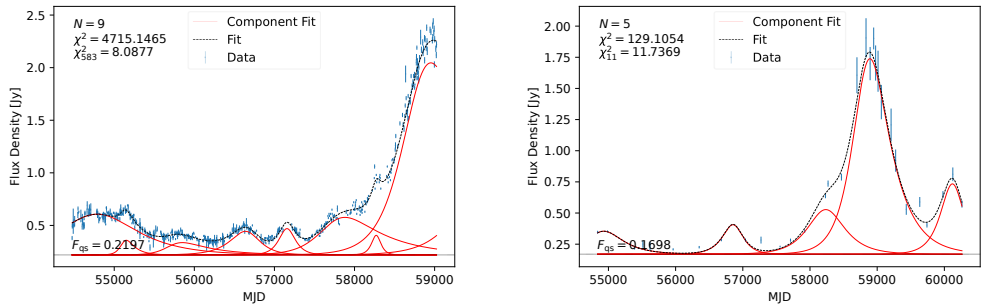

(a) Flare decomposition of the OVRO SD light curve (b) Flare decomposition of the VLBA Core light curve

Fig. 3: The light curve (blue dots) and decomposed model flare curves (red solid line) fitted with Equation 6. The black dashed line represents the sum of all model flares and the quiescent flux density $F_{\rm qs}$.

(M) and stopped the fitting with two criteria such as chi–square and a signal–to–noise ratio (SNR) of the core region. SNR is defined by SNR = $S_{\rm peak}/\sigma_{\rm rms}$, where $S_{\rm peak}$ is the peak flux density of the model component, and $\sigma_{\rm rms}$ is root–mean–square (RMS) in the region to be the combined area of the model component and the clean beam area constrained by FWHM. When there is no significant SNR improvement, we stopped the fitting when the sum of the reduced visibility chi–square and the reduced closure–phase chi–square improvement is less than 10 %. However, even though the chi–square improvement is less than 10 %, we added an additional component when the core region SNR was improved by a factor of ≥ 3 since we are interested in the core flux density and FWHM. The best fitting Gaussian model components were obatained only when the angular sizes FWHM ($\theta_{\rm FWHM}$) are larger than the minimum resolvable angular size. The minimum resolvable angular size $\theta_{\rm min}$ of an a Gaussian component in a natural–weighting image is determined, following Lobanov (2005), as

$$\theta_{\rm min} = \frac{4}{\pi}\left[\pi\theta^2_{\rm FWHM}\ln 2\ln\left(\frac{\rm SNR}{\rm SNR-1}\right)\right]^{1/2}. \quad (5)$$

We found that the source has a core–jet structure with the Core total flux density ($S_{\rm tot}$) ranging from 0.169±0.005 Jy to 1.906 ± 0.517 Jy, and the Core $\theta_{\rm FWHM}$ in a range of 0.036—0.228 milli–arcsecond (mas) within its uncertainties 1.78—13.4 %. As shown in Figure 2, the Core shows a giant flare peaking on MJD 58834 and the two jet components (Jet2 and Jet3) show flux enhancements with their peak on MJD 59433 and MJD 59275, respectively.

2.2. Flare Decomposition of 15 GHz OVRO 40 m SD light curve

We performed a flare decomposition using the OVRO SD and VLBA Core light curve as shown in Figure 2. We used the python package Dnest4 (Brewer & Foreman-Mackey 2018) that proceeds Bayesian inference with diffusive nested sampling. Light curves are supposed to consists of multiple exponential flares as follows (Kang et al. 2021)

$$F(t) = 2\sum_{j=1}^{N} A_j\left(\exp\left[\frac{t_{A,j}-t}{\tau_j}\right] + \exp\left[\frac{t-t_{A,j}}{s_j\tau_j}\right]\right)^{-1} + F_{\rm qs}. \quad (6)$$

t_A [MJD]	τ [day]	A [Jy]	s
OVRO SD			
$54776.3^{+0.3}_{-0.3}$	$425.83^{+0.82}_{-0.55}$	$0.3871^{+0.0010}_{-0.0010}$	$1.053^{+0.008}_{-0.009}$
$55122.3^{+1.0}_{-1.2}$	$48.95^{+2.03}_{-2.12}$	$0.1286^{+0.0013}_{-0.0017}$	$2.299^{+0.061}_{-0.095}$
$55735.4^{+0.0}_{-0.6}$	$114.50^{+2.92}_{-1.38}$	$0.0988^{+0.0012}_{-0.0020}$	$3.592^{+0.065}_{-0.134}$
$56658.6^{+1.7}_{-1.1}$	$186.24^{+0.74}_{-1.05}$	$0.2223^{+0.0012}_{-0.0009}$	$0.777^{+0.023}_{-0.025}$
$57154.7^{+0.4}_{-0.0}$	$87.69^{+0.17}_{-0.55}$	$0.2499^{+0.0023}_{-0.0015}$	$1.050^{+0.015}_{-0.022}$
$57738.4^{+0.6}_{-1.4}$	$198.37^{+1.61}_{-1.65}$	$0.3207^{+0.0017}_{-0.0014}$	$2.663^{+0.007}_{-0.011}$
$58272.5^{+1.1}_{-1.1}$	$53.32^{+0.04}_{-0.14}$	$0.1860^{+0.0060}_{-0.0069}$	$0.939^{+0.023}_{-0.035}$
$58808.4^{+0.3}_{-0.6}$	$223.94^{+0.55}_{-0.38}$	$1.6640^{+0.0043}_{-0.0056}$	$2.472^{+0.079}_{-0.057}$
$59491.1^{+1.0}_{-0.0}$	$266.88^{+3.04}_{-1.97}$	$0.5697^{+0.0083}_{-0.0075}$	$2.160^{+0.831}_{-0.934}$
VLBA Core			
$54899.6^{+39.6}_{-35.7}$	$212.71^{+37.89}_{-46.92}$	$0.1828^{+0.0103}_{-0.0083}$	$1.300^{+0.317}_{-0.242}$
$56865.9^{+22.9}_{-198.4}$	$148.70^{+21.30}_{-26.54}$	$0.2356^{+0.2177}_{-0.0357}$	$0.836^{+1.012}_{-0.137}$
$58223.8^{+37.9}_{-24.4}$	$233.09^{+13.16}_{-19.40}$	$0.3575^{+0.0292}_{-0.0254}$	$1.096^{+0.417}_{-0.305}$
$58840.1^{+40.8}_{-19.5}$	$193.37^{+5.98}_{-8.17}$	$1.5311^{+0.0871}_{-0.0726}$	$1.561^{+0.105}_{-0.147}$
$60123.2^{+14.3}_{-109.8}$	$157.88^{+46.32}_{-15.37}$	$0.5640^{+0.0372}_{-0.4192}$	$0.955^{+0.363}_{-0.191}$

Table 2: Peak date (t_A), timescale (τ), maximum flux density (A), and skewness (s) for each decomposed flare in the OVRO SD and VLBA Core light curves.

N is the number of flares and $F_{\rm qs}$ is the quiescent flux density. Each flare has four parameters such as the peak flux density A_j, the peak time $t_{A,j}$, the rising timescale τ_j and the skewness s_j which is the ratio between decaying and rising timescale of the $j^{\rm th}$ flare. The decomposed flares are shown in Figure 4a and Figure 4b, and parameters are listed in Table 2. Errors of parameters are estimated as 1–sigma confidence intervals of posterior distributions approximated to the Gaussian. The largest flare peaked on MJD $58808.4^{+0.4}_{-0.6}$ with $\tau = 233.94^{+0.55}_{-0.38}$ day and $A = 1.6640^{+0.0043}_{-0.0056}$ Jy in the OVRO SD light curve and peaked on MJD $58840.1^{+40.8}_{-19.5}$ with $\tau = 193.37^{+5.98}_{-8.17}$ day and $A = 1.5311^{+0.0871}_{-0.0726}$ Jy in the VLBA Core light curve.

3. Distance Measurements and Conclusions

We assumed that the radio variability timescale can be used to estimate the radius of the emission region, having the scaling factor $g = 1$ in Equation 1 and Equation 3. Since the VLBA Core is expected to be op-

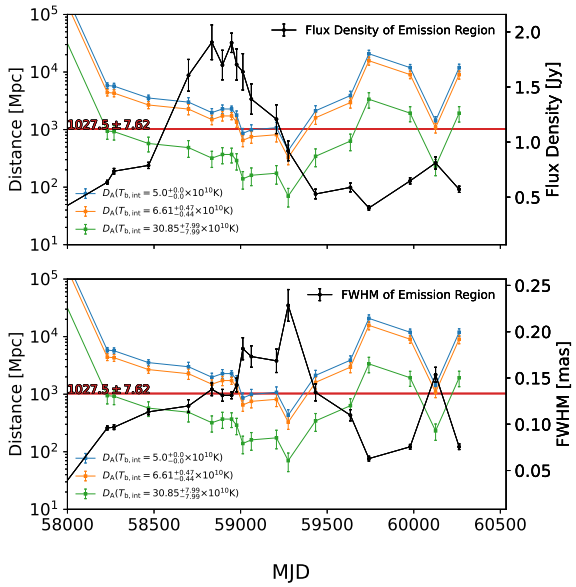

Fig. 5: Angular diameter distance measurements: blue, orange, and green solid lines represent distances calculated with Equation 2 for $T_{\rm b,int} = 5 \times 10^{10}$ K, $T_{\rm b,int} = 6.61^{+0.47}_{-0.44} \times 10^{10}$ K and $T_{\rm b,int} = 3.08 \pm 0.80 \times 10^{11}$ K, respectively. Red horizontal lines indicate the ΛCDM model's angular diameter distance for TXS 0506+056. The top panel show VLBA Core flux density curve, and the bottom panel show VLBA Core FWHM curves (black solid lines).

tically thick, we assumed that the VLBA Core has an uniform disk morphology, hence the scaling factor $K = \pi$ and $M = 0.8$ (Table 1). We used the OVRO SD timescale $\tau = 233.94^{+0.55}_{-0.38}$ and $\Delta S_\nu = 1.737 \pm 0.158$ Jy as the VLBA Core $S_{\rm tot}$ varies between the maximum and minimum flux density. We supposed three intrinsic brightness temperature $T_{\rm b,int}$ such as the equipartition brightness temperature ($T_{\rm b,int} = 5 \times 10^{10}$ K, Readhead 1994) and the mean brightness temperatures of distributions from VLBA samples ($T_{\rm b,int} = 6.61^{+0.47}_{-0.44} \times 10^{10}$ K, closely following Cheong et al., in prep.) and OVRO samples ($T_{\rm b,int} = 3.08 \pm 0.80 \times 10^{11}$ K, rescaled from Liodakis et al. 2018 since different Hubble constant) at Hubble constant $H_0 = 67.4 \pm 0.5$ km/s/Mpc with a matter density parameter $\Omega_{\rm M} = 0.315 \pm 0.007$. The results of distance measurements are shown in Figure 5. When constraining $T_{\rm b,int}$ from 5×10^{10} K to $3.08 \pm 0.80 \times 10^{11}$ K, consistent distance measurements with ΛCDM model are shown from MJD 58230 to MJD 59207 within the uncertainty of 11.07—24.25 %, where the VLBA Core $\theta_{\rm FWHM}$ is ranging in 0.096—0.182 mas within the uncertainty 2.12—7.50 %.

4. Discussions

The flare decomposition parameters of OVRO SD are much more precise than those for the VLBA Core since the data cadence is denser and the flux density errors are lower. Mean parameters of the largest flares have a slight difference between OVRO SD and VLBA Core. This discrepancy may arise from the truncation of the OVRO SD light curve during a critical flaring event. However, the most dominant factor affecting the distance measurements is $\theta_{\rm FWHM}$, because the distance depends on $\theta^{-3}_{\rm FWHM}$ (Equation 2). Thus, it is crucial to tightly constrain $\theta_{\rm FWHM}$ with minimal error and to ascertain when $\theta_{\rm FWHM}$ accurately reflects the intrinsic size of the emission region. However, the optimal flare phase for core size measurement varies depending on the supposed $T_{\rm b,int}$. As shown in Figure 5, results consistent with ΛCDM model are observed both before and after the peak of the largest flare, whose timescale is used in the distance measurements. Since $T_{\rm b,int} = 3.08 \pm 0.80 \times 10^{11}$ K is measured from flat spectrum radio quasar (FSRQ) samples, the BL Lac object TXS 0506+056 may be different from this intrinsic brightness temperature. To validate blazars as reliable tools for distance measurement, it is necessary to obtain $T_{\rm b,int}$ from blazar samples of the same class with prominent flares and confirm that the method used in this study yields consistent results across similar sources.

Acknowledgements. This research has made use of data from the MOJAVE database that is maintained by the MOJAVE team (Lister et al. 2018) This research has made use of data from the OVRO 40-m monitoring program (Richards, J. L. et al. 2011, ApJS, 194, 29), supported by private funding from the California Insitute of Technology and the Max Planck Institute for Radio Astronomy, and by NASA grants NNX08AW31G, NNX11A043G, and NNX14AQ89G and NSF grants AST-0808050 and AST- 1109911.

References

Abdollahi, S., Ajello, M., Ballet, J., et al. 2023, ApJS, 265, 31
Aghanim, N., Akrami, Y., Ashdown, M., et al. 2020, A&A, 641, A6
Brewer, B. J., & Foreman-Mackey, D. 2018, JSS, 86, 7
Hodgson, J. A., Marscher, A. P., Jorstad, S. G., et al. 2023, MNRAS, 521, L44–L47
Hovatta, T., Liodakis, I., Huppenkothen, D., et al. 2021, A&A, 650, A83
Kang, S., Rani, B., Krichbaum, T. P., et al. 2021, A&A, 651, A74
Liodakis, I., Romani, R. W., Filippenko, A. V., et al. 2018, ApJ, 866, 137
Lister, M. L., Aller, M. F., Aller, H. D., et al. 2018, ApJS, 234, 12
Lobanov, A. P. 2005, arXiv preprint, arXiv:astro-ph/0503225v1
Readhead, C. S. 1994, ApJ, 426, 51
Richards, J. L., Hovatta, T., Max-Moerbeck, W., et al. 2011, ApJS, 194, 29
Riess, A. G., Yuan, W., Macri, L. M., et al. 2022, ApJL, 934, L7
Scolnic, D. M., Jones, D. O., Rest, A., et al. 2018, ApJ, 859, 101
Verde, L., Schöneberg, N., & Gil-Marín, H. 2024, ARA&A, 62, 287
Zhang, Y., Perley, R. A., Carilli, C. L., et al. 2022, ApJ, 937, 19